Title

Elastic properties of Fe-bearing Akimotoite at mantle conditions: Implications for composition and temperature in lower mantle transition zone.

Journal

Fundamental Research, 2(4)

Authors

Zhao, Yajie

Wu, Zhongqing

Hao, Shangqin

et al.

Publication Date

2022-07-01

DOI

10.1016/j.fmre.2021.12.013

Peer reviewed

Fundamental Research 2 (2022) 570–577

Contents lists available at ScienceDirect

Fundamental Research

journal homepage: http://www.keaipublishing.com/en/journals/fundamental-research/

Article

Elastic properties of Fe-bearing Akimotoite at mantle conditions: Implications for composition and temperature in lower mantle transition zone

Yajie Zhao [a], Zhongqing Wu [a,b,c,*], Shangqin Hao [a,d], Wenzhong Wang [e,f], Xin Deng [a], Jian Song [a]

[a] Laboratory of Seismic and Physics of Earth's Interior, School of Earth and Space Sciences, University of Science and Technology of China, Hefei 230026, China
[b] National Geophysical Observatory at Mengcheng, University of Science and Technology of China, Hefei, China
[c] CAS Center for Excellence in Comparative Planetology, USTC, Hefei 230026, China
[d] Institute of Geophysics and Planetary Physics, Scripps Institution of Oceanography, University of California San Diego, La Jolla 92092, CA, USA
[e] Department of Earth Sciences, University College London, London WC1E 6BT, United Kingdom
[f] Earth and Planets Laboratory, Carnegie Institution for Science, Washington, DC 20015, USA

ARTICLE INFO

Article history:
Received 9 September 2021
Received in revised form 18 November 2021
Accepted 21 December 2021
Available online 21 January 2022

Keywords:
Akimotoite
Pyrolite
Elastic moduli
Temperature heterogeneity
Gaussian distribution

ABSTRACT

The pyrolite model, which can reproduce the upper-mantle seismic velocity and density profiles, was suggested to have significantly lower velocities and density than seismic models in the lower mantle transition zone (MTZ). This argument has been taken as mineral-physics evidence for a compositionally distinct lower MTZ. However, previous studies only estimated the pyrolite velocities and density along a one-dimension (1D) geotherm and never considered the effect of lateral temperature heterogeneity. Because the majorite-perovskite-akimotoite triple point is close to the normal mantle geotherm in the lower MTZ, the lateral low-temperature anomaly can result in the presence of a significant fraction of akimotoite in pyrolitic lower MTZ. In this study, we reported the elastic properties of Fe-bearing akimotoite based on first-principles calculations. Combining with literature data, we found that the seismic velocities and density of the pyrolite model can match well those in the lower MTZ when the lateral temperature heterogeneity is modeled by a Gaussian distribution with a standard deviation of ~100 K and an average temperature of dozens of K higher than the triple point of $MgSiO_3$. We suggest that a harzburgite-rich lower MTZ is not required and the whole mantle convection is expected to be more favorable globally.

1. Introduction

The pyrolite model proposed by Ringwood [1] has been widely used as a reference for the upper-mantle composition. Previous studies suggested that the velocities and density of the pyrolite model can match the one-dimension (1D) seismological models such as PREM [2] and AK135 [3] for the upper mantle [4] and the lower mantle [5,6]. However, the shear wave velocity and density of the pyrolite model are lower than PREM or AK135 up to 4% and 2% in the lower mantle transition zone (MTZ) [7–9]. Based on the complicated slab dynamics in the lower MTZ, different hypotheses including the enrichment of harzburgite-rich materials were introduced to reconcile this discrepancy [8,9].

The velocities and density of the pyrolite model in previous studies were only estimated along the 1D geotherm. The temperature lateral heterogeneity clearly indicated by the seismic tomography model [10–13] is ignored in the calculations. In general, this neglection will not affect the estimates of velocities and density because the velocities and density of minerals both depend near-linearly on the temperature. However, when the temperature heterogeneity can affect the mineral phases, the conventional method to calculate the velocities and density of the pyrolite model along the geotherm becomes inappropriate because this method did not include the effect of the phase transition on the velocities and density. The lower MTZ, where the calculated velocities and density of the pyrolite model using the conventional method fail to match the PREM and AK135 model, locates just the depth range where the temperature heterogeneity can significantly change the mineral phases in the pyrolite model (Fig. 1a). The majoritic garnet-akimotoite and akimotoite-bridgmanite phase transition occur at ~21-23 GPa and ~23-27 GPa [14–16] respectively, which correspond to the depths of the lower MTZ. The phase transition temperatures are close to the normal geotherm [17–19]. If low-temperature anomalies exist laterally, the pyrolite model will be expected to consist of a significant fraction of akimotoite. Can a pyrolite composition explain the

* Corresponding author.
E-mail address: wuzq10@ustc.edu.cn (Z. Wu).

https://doi.org/10.1016/j.fmre.2021.12.013

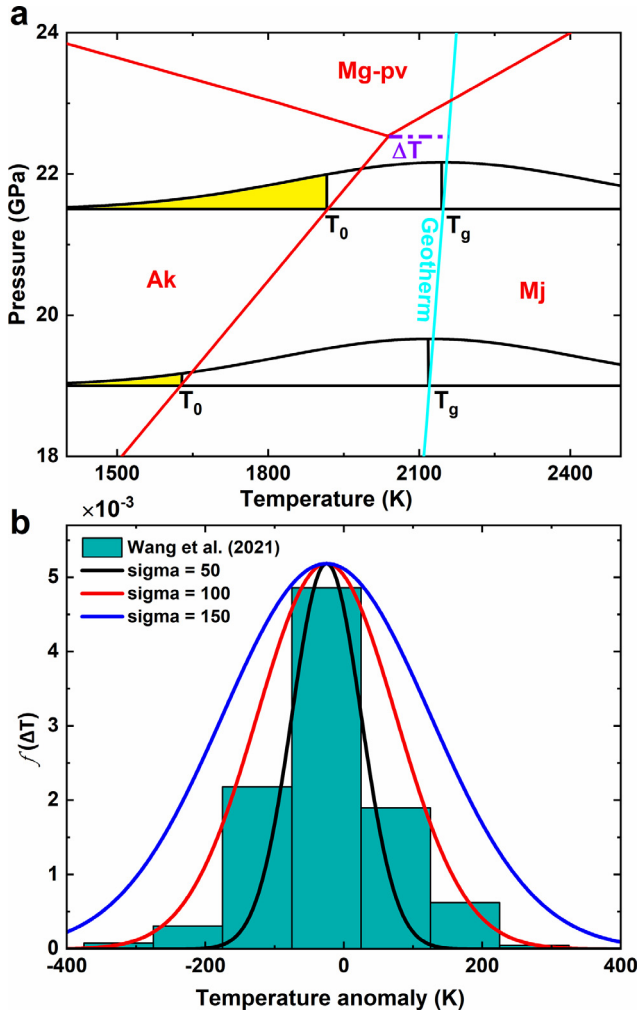

Fig. 1. The lateral temperature distribution in the lower MTZ. (a) Schematic diagram of calculating volume proportion of akimotoite by $MgSiO_3$ phase diagram with Gaussian distribution. Red lines are the phase boundary from Ishii et al. [17]. The cyan line represents the normal mantle geotherm. Black lines represent the Gaussian distribution of temperature at two depths. The yellow shaded parts represent the temperature where akimotoite exists. ΔT is the temperature difference between geotherm T_g and triple point of the $MgSiO_3$ phase transition. (b) Comparison of distributions of temperature anomaly from Wang et al. [11] and Gaussian distribution of different σ.

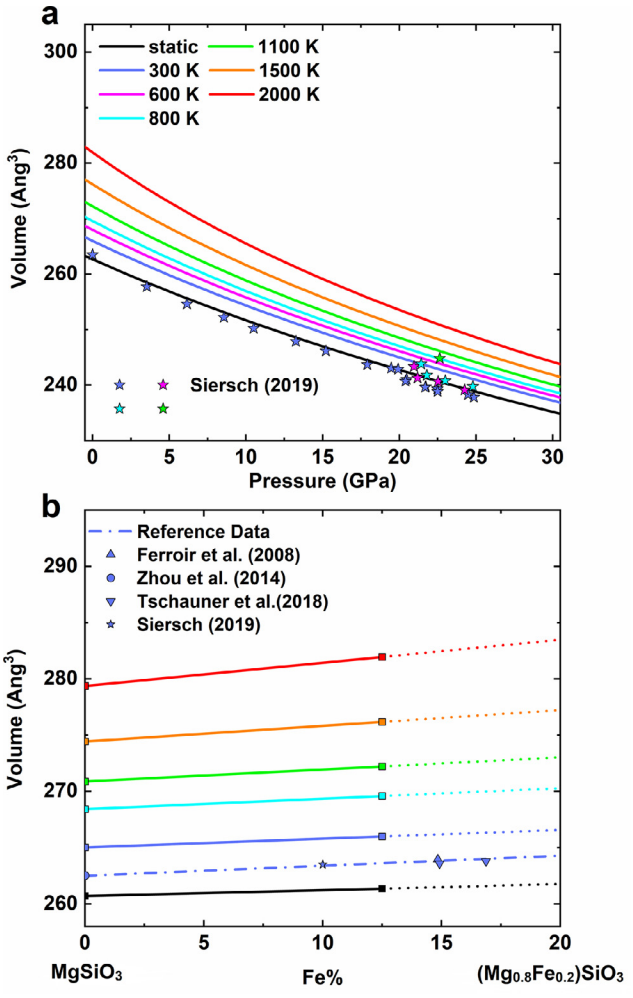

Fig. 2. The volumes of akimotoite at various pressures, temperatures, and Fe content. (a) Equation of states of akimotoite. The solid lines represent our calculation results for $Mg_{0.875}Fe_{0.125}SiO_3$, and the solid scatters are for $Mg_{0.9}Fe_{0.1}SiO_3$ from Siersch [9]. (b) Effect of Fe content on volume of akimotoite in different temperatures at 0 GPa. Solid lines are fitted by volume of $MgSiO_3$ akimotoite [26] and $Mg_{0.875}Fe_{0.125}SiO_3$ (this study), and the dotted lines represent the extrapolation. Dot-dashed line is fitted by experiment data [9,20,57,58].

velocities and density of the lower MTZ after including the mineral phase variations? Does mineral physics require a harzburgite-rich lower MTZ?

The answers to the questions, which have fundamental implications to the mantle convection, require the elastic properties of iron-bearing akimotoite at high pressures and temperatures. The equation of states and elastic properties of $MgSiO_3$ akimotoite have been investigated by previous studies [20–28]. The sound velocities of the iron-bearing akimotoite $(Mg_{0.9},Fe_{0.1})SiO_3$ have been measured by Siersch [9] up to 26 GPa and 1100 K using ultrasonic interferometry and synchrotron X-ray diffraction. However, the velocities and density of iron-bearing akimotoite at MTZ conditions remain unknown.

In this study, we investigated the elastic properties of $(Mg_{0.875},Fe_{0.125})SiO_3$ akimotoite at mantle conditions using first-principles calculations. The calculated results are consistent with the available experimental data. The temperature heterogeneity in the lower MTZ will affect the volume proportion of akimotoite and hence the velocities and density of the pyrolite model. Combining our results with the elastic properties of other minerals, we calculated the velocities and density of the pyrolite model in the lower MTZ with the effect of temperature heterogeneity and compared mineral-physics results with seismic reference models.

2. Material and methods

2.1. First-principles calculations

The calculations were performed using the Quantum Espresso package [29] based on the density functional theory (DFT) [30]. The local density approximation (LDA) was adopted for exchange-correlation potential [31,32]. The pseudopotential for magnesium was generated by von Barth and Car [33], and the iron pseudopotential was generated using the method of Vanderbilt [34]. The pseudopotentials for oxygen and silicon were generated by Troullier and Martins [35]. The plane wave kinetic energy and charge density cutoff were 70 Ry and 700 Ry, respectively. The initial structure for $(Mg_{1-x},Fe_x)SiO_3$ akimotoite with $x = 0.125$ (akimotoite refers to the composition of $(Mg_{0.875},Fe_{0.125})SiO_3$

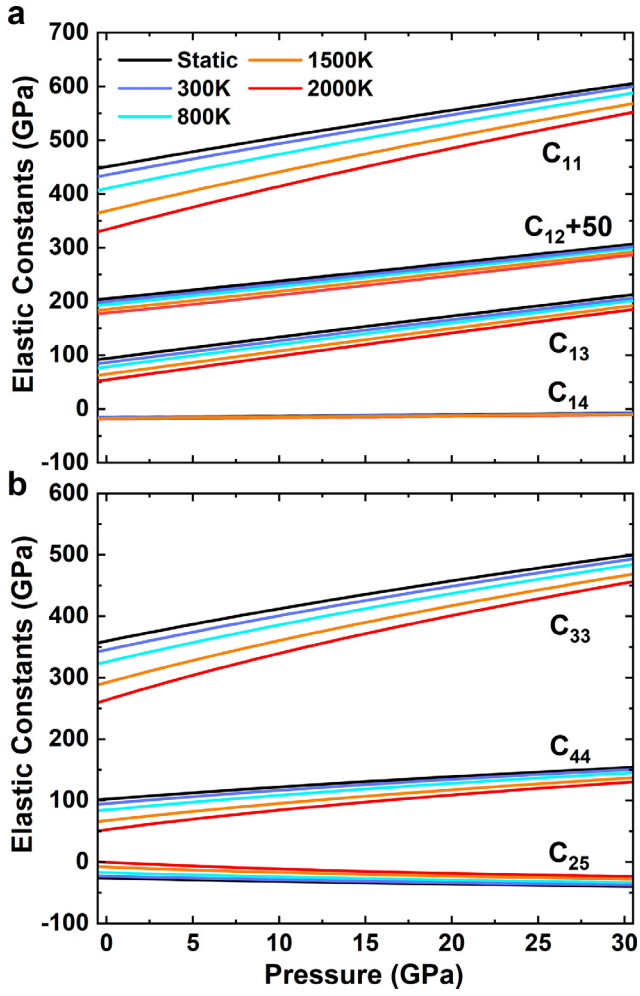

Fig. 3. Pressure dependences of elastic constants of akimotoite at various temperatures.

hereafter unless otherwise specified) is generated by replacing a Mg atom with iron in a 40-atoms unit cell. The akimotoite structures at different pressures were optimized with a $2\times2\times2$ k-point mesh by using damped variable cell shape molecular dynamics [36]. The dynamical matrices were calculated using the density functional perturbation theory (DFPT) [37] to obtain vibrational frequencies at a $2\times2\times2$ q-point mesh for each optimized structure.

2.2. Elasticity and anisotropy calculations

Isothermal elastic tensors are determined by second derivative of free energy with strain from Eq. 1 [38]:

$$C^{T}_{ijkl}=\frac{1}{V}\left(\frac{\partial^2 F}{\partial e_{ij}\partial e_{kl}}\right)+\frac{1}{2}P\left(2\delta_{ij}\delta_{kl}-\delta_{il}\delta_{kj}-\delta_{ik}\delta_{jl}\right) \tag{1}$$

Helmholtz free energy at volume V with infinitesimal strains e_{ij} (i,j=1,2,3) can be obtained from the quasi-harmonic approximation:

$$F(V,T,e_{ij})=U_0(V,e_{ij})+\sum_{q,m}\frac{\hbar\omega_{qm}(V,e_{ij})}{2}+K_BT\sum_{q,m}ln\left\{1-exp\left[-\frac{\hbar\omega_{qm}(V,e_{ij})}{k_BT}\right]\right\} \tag{2}$$

The $\omega_{q,m}$ represents vibrational frequency of the normal mode m at phonon wave vector q. $\hbar$ and K_B are the Planck and Boltzmann constants, respectively. Thus, the conventional method for elastic properties calculations requires vibrational frequencies at numerous strained configurations, which need a large amount of computation. In this study, we adopted the method proposed by Wu and Wentzcovitch [39], which only requires vibrational density of states of unstrained configurations and elastic tensors at static conditions. This method reduces the computation to one tenth of the conventional method and maintains accuracy. The method has been successfully applied to many minerals [4,26,40-45].

Based on Kelvin-Christoffel equation, we can obtain the wave velocities propagating in different directions:

$$\left|C_{ijkl}n_jn_l-\rho V^2\delta_{ik}\right|=0 \tag{3}$$

where n=(n_1, n_2, n_3) is the vector of propagation direction, C_{ijkl} is the four-order elastic tensor, ρ presents the density, and V is the wave velocity. The P wave anisotropy (A_P), S wave anisotropy (A_S), and maximum polarization anisotropy (A_S^{po}) are defined as:

$$A_P=2\times\frac{(V_P^{max}-V_P^{min})}{(V_P^{max}+V_P^{min})} \tag{4a}$$

$$A_S=2\times\frac{(V_S^{max}-V_S^{min})}{(V_S^{max}+V_S^{min})} \tag{4b}$$

$$A_S^{po}=2\times\frac{(V_{S1}-V_{S2})_{max}}{(V_{S1}+V_{S2})} \tag{4c}$$

2.3. Geophysical modeling

The pyrolite model along the normal geotherm contains ~56 vol.% ringwoodite ($(Mg,Fe)_2SiO_4$), ~39 vol.% majoritic garnet ($(Mg,Fe,Ca)_3(Mg,Si,Al)_2Si_3O_{12}$), and ~5 vol.% Davemaoite ($CaSiO_3$) in the lower MTZ [46–50]. The Fe/(Fe+Mg) of the pyrolite model is ~11 mol.% [51]. The iron partition coefficients K_D of garnet-ringwoodite, akimotoite-ringwoodite, ringwoodite-ferropericlase, and bridgmanite-ferropericlase are around 0.8, 0.4, 0.65, and 0.7, respectively [14,17,52-54]. Based on the total iron content in the pyrolite model and partition coefficients between different minerals, the Fe/(Fe + Mg) in ringwoodite, garnet, akimotoite, and bridgmanite is ~10 mol.%, ~8 mol.%, ~4 mol.%, and ~10 mol.% respectively. The iron content of the majoritic garnet estimated in this study is closed to those from Irifune et al. [7] (~7 mol.%). Based on the chemical composition of garnet (pyrolite minus olivine) from Irifune et al. [7], the majoritic garnet is $Py_{15}Gr_{26}Alm_7Mj_{52}$ with ~15 vol.% pyrope [40], ~26 vol.% grossular [4], ~7 vol.% almandine [55], and ~52 vol.% majorite at 20 GPa, which is similar to Arimoto et al. [55] and Pamato et al. [8]. The chemical composition of majoritic garnet varies with depth mainly because of the exsolution of Davemaoite. In the lower MTZ, the majoritic garnet is $Py_{31}Gr_{10}Alm_8Mj_{51}$ since there is ~5 vol.% Davemaoite transformed from majoritic garnet. The elastic modulus and density of the pyrolite model are calculated using Eqs. 5, 6 [56]:

$$\mathrm{M}=\left[\sum_i f_i\mathrm{M_i}+\left(\sum_i f_iM_i^{-1}\right)^{-1}\right]/2 \tag{5}$$

$$\rho=\sum_i f_i\rho_i \tag{6}$$

where f_i, ρ_i, and M_i are the volume fraction, density, and moduli of the ith mineral, respectively.

The temperature lateral heterogeneity will change the mineral phase in the lower MTZ. To investigate this effect on the velocities and density of the pyrolite model, we assume a Gaussian temperature distribution for the temperature heterogeneity of an entire spherical layer at a certain depth:

$$f\left(\mathrm{T};T_g,\sigma\right)=\frac{1}{\sigma\sqrt{2\pi}}\exp\left(-\frac{(T-T_g)^2}{2\sigma^2}\right) \tag{7}$$

Table 1
Equation of state parameters of akimotoite at 0 GPa.

Reference	Composition	T (K)	V_0 (Å^3)	K_T (GPa)	$(\partial K_T/\partial P)_T$
This study	$Mg_{0.875}Fe_{0.125}SiO_3$	Static	262.7	213.2	4.35
This study	$Mg_{0.875}Fe_{0.125}SiO_3$	300	266.0	202.4	4.49
This study	$Mg_{0.875}Fe_{0.125}SiO_3$	1000	271.3	180.1	4.77
This study	$Mg_{0.875}Fe_{0.125}SiO_3$	2000	282.0	141.3	5.40
Seirsch (2019)	$Mg_{0.9}Fe_{0.1}SiO_3$	300	263.5	197	5.3
Hao et al. (2019)	$MgSiO_3$	300	265.2	202	4.40
Seirsch et al. (2021)	$MgSiO_3$	300	262.43	205	4.9

K_T: the isothermal bulk modulus at 0 GPa.

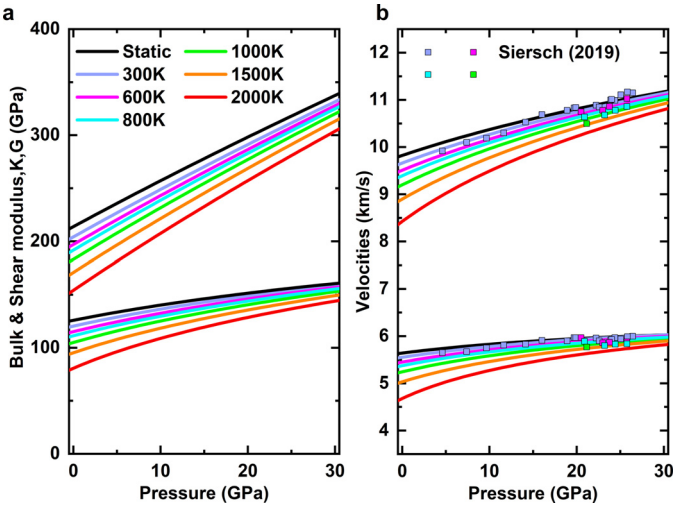

Fig. 4. Pressure dependences of (a) bulk and shear modules and (b) velocities at various temperatures. Experimental data source: squares, Siersch [9].

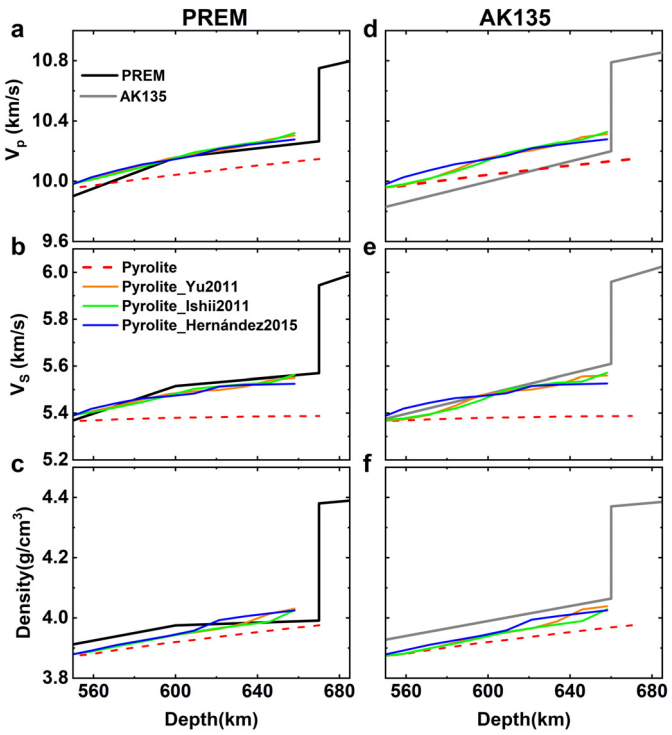

Fig. 5. (a and d) Compressional wave velocities V_P, (b and e) shear wave velocities V_S, and (c and f) densities of pyrolite model and seismic models. The black and grey lines represent PREM [2] and AK135 [3] model respectively. The red dashed lines represent pyrolite along the normal geotherm. The orange, green and blue lines are the results of pyrolite with temperature heterogeneity corresponding to the smallest misfit functions D_{all} based on the phase boundary of Yu et al. [19], Ishii et al. [17], and Hernández et al. [18] respectively. (a-c) are the fitting results based on PREM and (d-f) are the fitting results based on AK135.

Here, T_g is the normal geothermal temperature and σ is the standard deviation of mantle temperature. The ratio of akimotoite is determined by

$$y(T_0;T_g,\sigma)=\frac{1}{\sigma\sqrt{2\pi}}\int_{-\infty}^{T_0}\exp\left(-\frac{(T-T_g)^2}{2\sigma^2}\right)dT \quad (8)$$

Here, T_0 is temperature at which garnet transforms to akimotoite or akimotoite transforms to bridgmanite (Fig. 1a). The degree to which the pyrolite model matches the V_P, V_S and density is evaluated using the misfit function D_{all}:

$$D_{all}=\sqrt{\frac{\sum_{i=1}^{n}\left(\left(\frac{V_{Pi}^{py}}{V_{Pi}^{model}}-1\right)^2+\left(\frac{V_{Si}^{py}}{V_{Si}^{model}}-1\right)^2+\left(\frac{\rho_i^{py}}{\rho_i^{model}}-1\right)^2\right)}{3n}} \quad (9)$$

where V_{Pi}^{py}, V_{si}^{py}, ρ_i^{py}, V_{Pi}^{model}, V_{si}^{model} and ρ_i^{model} represent the P- and S-wave velocities and density of the pyrolite model and seismic models, respectively, and n is the number of data points.

3. Results and discussion

3.1. Elastic properties of akimotoite at high pressures and temperatures

The equation of states of akimotoite up to 30 GPa and 2000 K are shown in Fig. 2a and listed in Table 1. The calculated volume at ambient temperature is ~1.5% larger than the previous experimental measurements [9]. It was observed that such discrepancies between calculations and experiments dwindled away while the pressure and the temperature increased. At MTZ's pressure, the relative differences of volume are less than 0.5% at 1100 K. The volume of akimotoite increases linearly with iron concentration [9,20,57,58]. The effect of iron content on volume (Fig. 2b), which is estimated based on $MgSiO_3$ akimotoite from Hao et al. [26] and $(Mg_{0.875},Fe_{0.125})SiO_3$ akimotoite in this study, agrees well with the experimental data at ambient conditions.

Akimotoite has a trigonal structure, and its elastic tensor can be determined by seven independent parameters C_{11}, C_{12}, C_{13}, C_{14}, C_{25}, C_{33}, and C_{44} (Fig. 3, Table S1 and S2). The adiabatic bulk moduli K_S and shear moduli G are calculated based on the Voigt-Reuss-Hill average [56] (Fig. 4a). The derivatives of elastic modulus with respect to PT are listed in Tables S1 and S2. The compression wave velocity V_P and shear wave velocity V_S are given by $V_P=\sqrt{\frac{K_S+\frac{4}{3}G}{\rho}}$ and $V_S=\sqrt{\frac{G}{\rho}}$, and their derivatives with respect to PT are shown in Fig. 4b and Table S3. The calculated wave velocities agree with those measured by Siersch [9] within ~1%.

The pressure dependences of anisotropies at various temperatures are shown in Fig. S1. The anisotropy of $MgSiO_3$ akimotoite is larger than other major minerals in the lower MTZ [26,27]. Our calculation shows that iron further increases the anisotropies of akimotoite. At 20 GPa and 1500 K, A_P, A_S, and A_S^{PO} of iron-bearing akimotoite are 2.2%, 6.4%, and 6.1% larger than $MgSiO_3$ akimotoite respectively. The differences of A_P, A_S, and A_S^{PO} between iron-bearing and $MgSiO_3$ akimotoite increase to 2.4%, 7.7%, and 7.4% respectively at 24 GPa and 2000 K.

Table 2
Bulk (Ks) and Shear (G) Moduli of minerals at base of the transition zone employed in the calculation of density and seismic velocities.

Composition	K_S (GPa)	$\partial K_S/\partial P$	$\partial K_S/\partial T$ (MPa/K)	$\partial^2 K_S/\partial P^2$ ($\times 10^{-3} GPa^{-1}$)	$\partial^2 K_S/\partial P \partial T$ ($\times 10^{-4} K^{-1}$)	$\partial^2 K_S/\partial T^2$ ($\times 10^{-6} GPa/K^2$)	Ref
Ringwoodite							
Mg_2SiO_4	184.9	4.23	-15.05	-8.25	0.54	-0.70	Cal.1
$(Mg_{0.875}Fe_{0.125})_2SiO_4$	186.9	4.79	-20.99	-21.61	3.43	-1.94	Cal.1
Garnet							
$Mg_3Al_2Si_3O_{12}$	176.3	3.79	-5.59	1.36	-8.88	4.85	Cal.2
$Ca_3Al_2Si_3O_{12}$	170.0	4.22	-8.01	-4.96	-1.70	0.48	Cal.3
$Fe_3Al_2Si_3O_{12}$	172.6	4.43	-18.7				Exp.1
$Mg_4Si_4O_{12}$	159.7	4.64	-14.70	-13.73	0.47	-0.27	
Akimotoite							
$MgSiO_3$	204.9	4.45	-17.72	-11.39	1.49	-1.18	Cal.4
$Mg_{0.875}Fe_{0.125}SiO_3$	205.1	4.62	-24.07	-13.71	4.35	-2.86	This study
Ca-perovskite							
$CaSiO_3$	248	4.2	-36				Exp.2
Bridgmanite							
$MgSiO_3$	247.5	4.00	-19.38	-4.96	1.03	-1.42	Cal.5
$Mg_{0.875}Fe_{0.125}SiO_3$	249.4	4.04	-19.56	-5.07	0.96	-1.37	Cal.5
	G (GPa)	$\partial G/\partial P$	$\partial G/\partial T$ (MPa/K)	$\partial^2 G/\partial P^2$ ($\times 10^{-3} GPa^{-1}$)	$\partial^2 G/\partial P \partial T$ ($\times 10^{-4} K^{-1}$)	$\partial^2 G/\partial T^2$ ($\times 10^{-6} GPa/K^2$)	
Ringwoodite							
Mg_2SiO_4	120.9	1.30	-10.96	-16.73	1.72	-0.39	Cal.1
$(Mg_{0.875}Fe_{0.125})_2SiO_4$	115.2	1.35	-13.06	-20.71	3.06	-1.02	Cal.1
Garnet							
$Mg_3Al_2Si_3O_{12}$	93.95	1.35	-6.48	-13.54	-3.76	2.76	Cal.2
$Ca_3Al_2Si_3O_{12}$	106.3	1.29	-6.03	-14.7	0.07	0.38	Cal.3
$Fe_3Al_2Si_3O_{12}$	94.2	1.06	-12.6				Exp.1
$Mg_4Si_4O_{12}$	83.53	1.28	-8.77	-14.19	0.97	-0.01	
Akimotoite							
$MgSiO_3$	128.1	1.79	-13.77	-17.13	2.26	-0.81	Cal.4
$Mg_{0.875}Fe_{0.125}SiO_3$	120.9	1.85	-17.58	-20.99	4.58	-2.28	This study
Ca-perovskite							
$CaSiO_3$	126	1.6	-15				Exp.2
Bridgmanite							
$MgSiO_3$	167.6	1.79	-19.8	-7.82	1.81	-1.21	Cal.5
$Mg_{0.875}Fe_{0.125}SiO_3$	164.6	1.79	-19.74	-8.34	1.85	-1.20	Cal.5

Cal.1 Núñez Valdez et al. [63], Cal. 2 Hu et al. [38], Cal. 3 Duan et al. [4], Cal. 4 Hao et al. [26], Cal.5 Shukla et al. [64], Exp. 1 Arimoto et al. [53], Exp. 2 Greaux et al. [65] . The data from calculations are fitted for the pressure and temperature range of 0-30 GPa and 270-2000 K respectively based on the equation: $M = M_0 + \frac{\partial M}{\partial P} \times P + \frac{\partial M}{\partial T} \times (T - 270) + \frac{\partial^2 M}{\partial P^2} \times P^2 + \frac{\partial^2 M}{\partial P \partial T} \times P \times (T - 270) + \frac{\partial^2 M}{\partial T^2} \times (T - 270)^2$. M represents the elastic moduli. P is pressure in GPa, and T is temperature in Kelvin.

3.2. The pyrolite model can account for the velocities and density of the lower MTZ

Combining the elasticities of akimotoite and other minerals in the lower MTZ (summarized in Table 2), we calculated the velocities and density of the pyrolite model along the normal geotherm. As shown in Fig. 5, the S-wave velocity of the pyrolite model in the lower MTZ is lower than PREM or AK135 up to 0.2 km/s, similar to previous studies [7,8]. The stagnant slabs in the lower MTZ may contain non-negligible harzburgite. However, the velocities of harzburgite with an initial composition of 81.5 vol.% wadsleyite and 18.5 vol.% majoritic garnet are still lower than the PREM or AK135 ~0.1 km/s unless the temperature in the lower MTZ is 200 K lower than the adiabat with a potential temperature of 1673 K [8]. The stable field of akimotoite is close to the mantle geotherm. The harzburgite mineral model can contain ~15 vol.% akimotoite at the temperature around 1673-1873 K [59,60]. Siersch [9] found that the velocities of harzburgite can match PREM and AK135 after including the contribution of the akimotoite phase. Their results suggested a pure harzburgite and a reference temperature below 1873 K for the lower MTZ. Although the presence of a harzburgite-rich layer at local regions is supported by the stagnant slabs in the lower MTZ, the mechanism for a global harzburgite layer in the lower MTZ remains unclear.

The above-mentioned velocities and density of pyrolite and harzburgite along geotherm were calculated based on the average temperature and the mineral phases at the average temperature. In general, ignoring the secular temperature distribution in Earth's interior does not affect the 1D velocity and density profiles since they depend near-linearly on temperature. However, in the lower MTZ where the stable field of akimotoite is close to the mantle geotherm, akimotoite can appear even geotherm is above the stable field of akimotoite and the akimotoite fraction is sensitive to the temperature distribution (Fig. 1a). Since akimotoite has much higher velocities than majoritic garnet especially V_S (Fig. S2) [26,27], the effect of akimotoite on the velocities and density of the pyrolite model cannot be ignored.

By assuming a Gaussian temperature distribution, we determined the volume proportion of akimotoite at the mantle geotherm T_g with different standard deviations (σ is 0~300) based on the $MgSiO_3$ phase diagram (see Fig. 1a and Eq. 8). Combining elastic data of minerals in the lower MTZ (Table 2), we obtained the velocities and density of the pyrolite model. The calculated misfit function D_{all} (Eq. 9) based on AK135 is shown in Fig. 6. ΔT is the temperature difference between T_g and the triple point of $MgSiO_3$ phase transition. The D_{all} increases dramatically once $\Delta T < 0\ K$, suggesting that the triple point of the phase transition should be below the geotherm, which is consistent with the perspective that majorite is a stable phase along geotherm. The results from the conventional method, which ignores the temperature distribution, are represented by those with $\sigma = 0\ K$. D_{all} with $\sigma = 0\ K$ for the cases with $\Delta T > 0\ K$ is ~1.7% for AK135. Introducing the temperature distribution can reduce D_{all} by ~40%. The same conclusions can be derived with D_{all} based on PREM (Fig. S3). As shown in Fig. 5, after considering the temperature distribution, the consistency between the velocities and

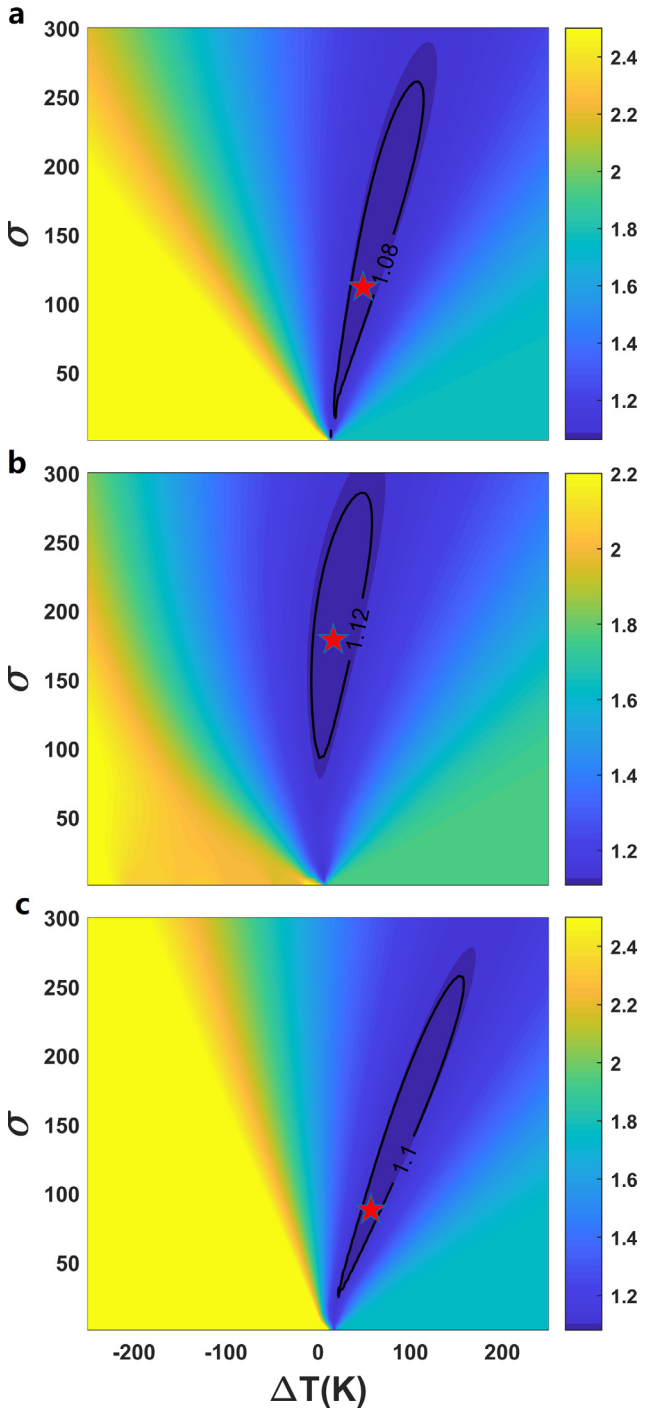

Fig. 6. The deviation D_{all} between pyrolite and AK135. The results are based on phase boundary of (a) Yu et al. [19], (b) Ishii et al. [17], and (c) Hernández et al. [18] at different σ and ΔT. Stars are the points of the smallest D_{all}.

density of the pyrolite model and those of PREM and AK135 at the depth range of 580-660 km is as good as or better than that at the depth range of 540-580 km. The harzburgite model contains only about 18.5 vol.% majoritic garnet. Introducing Gaussian distribution of temperature into the harzburgite model can only reduce D_{all} ~7% (Figs. S4 and S5), thus failing to match the velocities and density of PREM and AK135 at lower MTZ. Thus, our results demonstrate that the pyrolite model can explain well the velocities and density of the lower MTZ with temperature heterogeneity. The lower MTZ with a composition different from the upper mantle and lower mantle is not required.

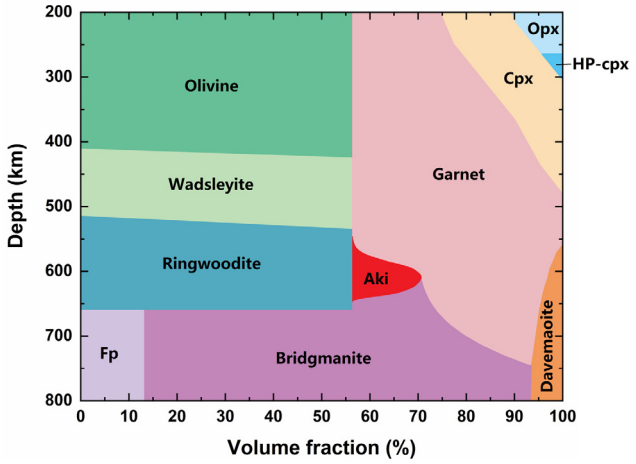

Fig. 7. The pyrolite model with temperature heterogeneity (modified from Frost [46]). Opx = Orthopyroxene, HP-cpx = High-pressure clinopyroxene, Cpx = Clinopyroxene, Aki = Akimotoite, Fp = Ferropericlase. The phase boundary of orthopyroxene to high-pressure clinopyroxene is from Akashi et al. [69]. Although akimotoite is stable below the geotherm, the pyrolytic lower MTZ can contain a significant amount of akimotoite because of the temperature heterogeneity (Fig. 1). The velocities and density of the pyrolite model agree well with the seismic results in the lower MTZ after considering the temperature heterogeneity (Fig. 5)

3.3. The temperature distribution of the lower MTZ

The smallest D_{all}^{AK135} occurs at $\Delta T = 49\ K$ and $\sigma = 112\ K$ for Yu et al. [19], at $\Delta T = 16\ K$ and $\sigma = 179\ K$ for Ishii et al. [17], and at $\Delta T = 57\ K$ and $\sigma = 88\ K$ for Hernández et al. [18], respectively. The best σ and ΔT derived from PREM are larger than those from AK135. Wang et al. [11] constrained the water and temperature distribution at the base of MTZ by combining 660-km topography and seismic tomography. The σ from their temperature distribution is around 100 (Fig. 1b), which is closed to σ our fitted based on AK135. These results suggest that the temperature in the lower MTZ can be described by a Gaussian distribution with a σ of ~ 100 K and an average temperature of dozens of K higher than the triple point of $MgSiO_3$. The conclusion is not sensitive to the iron partition coefficients K_D between akimotoite and ringwoodite (Table S4). The triple point of the $MgSiO_3$ phase diagram provides another anchor point for the mantle geotherm.

For the lower MTZ, $\sigma \sim 100\ K$ means that the volume proportions of mantle material with temperature 200 K lower than geotherm is ~2.25%. The cold mantle is mainly caused by subducting slabs. Assuming that all subducting slabs penetrate into the lower mantle except the flat slabs which are stagnant above the 660 km discontinuity, using the subduction length, the dip angle of slab, the width of stagnant flat slab for each slab beneath arc volcanoes [61–63] and the petrological model of the slab with a thickness of 80 km [48], we calculated the volume proportion of subducting slabs in the lower MTZ globally, ~2.88 vol.%. This may be overestimated since there are some young subducting slabs that have not been subducted to the lower MTZ yet. Considering only a fraction of the slab is 200 K lower than the ambient mantle, the estimation on volume proportion of slab is close to 2.25% in the lower MTZ and also supports that σ is ~ 100 K.

The temperature distribution allows ~10-15 vol.% akimotoite in the lower MTZ (Fig. 7). The strong elastic anisotropy of akimotoite (Fig. S1) provides a reasonable explanation for the anisotropy of the lower MTZ although ringwoodite and majoritic garnet, the major minerals in the lower MTZ, are almost isotropic. Global seismic observation shows that the radial anisotropy ($\xi = \frac{V_{SH}^2}{V_{SV}^2}$) of the lower MTZ is less than 2.3%

[64–66]. The anisotropy can be explained by no more than 5% akimotoite in the pyrolite model when the lattice of akimotoite is arranged in a preferred orientation completely. 10-15% akimotoite in the pyrolite model should be large enough to generate the weak anisotropy in lower MTZ. We updated the pyrolite model by considering the temperature heterogeneities (Fig. 7). The pyrolite model can well account for the seismic velocity profile in the lower MTZ. Thus, although the 660-km boundary partially blocks the circulation between the upper mantle and lower mantle as suggested by slab stagnant and 660-km topography at the short length scale [61,67,68] , a lower MTZ compositionally significantly different from the upper mantle and lower mantle is not a requisite. This is consistent with only part of slabs stagnant at the 660-km boundary. The 660-km boundary is not an efficient obstacle for mantle flow and the whole mantle convection is expected to be more favorable globally.

4. Conclusion

We investigate the elastic properties of akimotoite $(Mg_{0.875}, Fe_{0.125})SiO_3$ at high pressures and temperatures with first-principles calculations based on the density functional theory (DFT). The results are well consistent with available experimental data. In lower MTZ, the akimotoite is ~20% (11%) larger in V_S (V_P) than in majoritic garnet.

The volume proportion of akimotoite in a pyrolitic lower MTZ depends on the temperature heterogeneity. Combining the elasticity of akimotoite and other minerals in the MTZ, we estimate the velocity and density profiles of pyrolite with the Gaussian temperature distributions. We found that the velocities and density of pyrolite fit the seismic velocity profile well when the standard deviation of temperature for lower MTZ is ~100 K and the geotherm locates at a little bit above the triple point of the $MgSiO_3$ phase diagram. The triple point of the $MgSiO_3$ phase diagram provides another anchor point for geotherm. The presence of ~10-15 vol.% akimotoite at the base of MTZ provides a reasonable explanation for the anisotropy of the lower MTZ although the other major minerals in the lower MTZ are almost isotropic. A lower MTZ with composition significantly different from the pyrolite model is not a requisite and the whole mantle convection is expected to be more favorable globally.

Declaration of Competing Interest

The authors declare that they have no conflicts of interest in this work.

Acknowledgments

This work is supported by the Natural Science Foundation of China (Grants No. 41925017, 41721002) and the Fundamental Research Funds for the Central Universities (Grant No. WK2080000144). The computations were conducted in the Supercomputing Center of the University of Science and Technology of China.

Supplementary materials

Supplementary material associated with this article can be found, in the online version, at doi:10.1016/j.fmre.2021.12.013.

References

[1] A.E. Ringwood, Phase transformations and their bearing on the constitution and dynamics of the mantle, Geochim. Cosmochim. Acta 55 (1991) 2083–2110.
[2] A.M. Dziewonski, D.L. Anderson, Preliminary reference Earth model, Phys. Earth Planet. Inter. 25 (1981) 297–356.
[3] B.L. Kennett, E. Engdahl, R. Buland, Constraints on seismic velocities in the Earth from traveltimes, Geophys. J. Int. 122 (1995) 108–124.
[4] L. Duan, W. Wang, Z. Wu, et al., Thermodynamic and Elastic Properties of Grossular at High Pressures and High Temperatures: A First-Principles Study, Journal of Geophysical Research: Solid Earth 124 (2019) 7792–7805.
[5] Z. Zhang, L. Stixrude, J. Brodholt, Elastic properties of MgSiO3-perovskite under lower mantle conditions and the composition of the deep Earth, Earth Planet. Sci. Lett. 379 (2013) 1–12.
[6] Z. Wu, Velocity structure and composition of the lower mantle with spin crossover in ferropericlase, Journal of Geophysical Research: Solid Earth 121 (2016) 2304–2314.
[7] T. Irifune, Y. Higo, T. Inoue, et al., Sound velocities of majorite garnet and the composition of the mantle transition region, Nature 451 (2008) 814–817.
[8] M.G. Pamato, A. Kurnosov, T. Boffa Ballaran, et al., Single crystal elasticity of majoritic garnets: Stagnant slabs and thermal anomalies at the base of the transition zone, Earth Planet. Sci. Lett. 451 (2016) 114–124.
[9] N.C. Siersch, The effect of Fe and Al on the elasticity of akimotoite, (Doctoral dissertation) (2019).
[10] U. Meier, J. Trampert, A. Curtis, Global variations of temperature and water content in the mantle transition zone from higher mode surface waves, Earth Planet. Sci. Lett. 282 (2009) 91–101.
[11] W. Wang, H. Zhang, J.P. Brodholt, et al., Elasticity of hydrous ringwoodite at mantle conditions: Implication for water distribution in the lowermost mantle transition zone, Earth Planet. Sci. Lett. 554 (2021) 116626.
[12] F. Cammarano, B. Romanowicz, Insights into the nature of the transition zone from physically constrained inversion of long-period seismic data, Proc. Natl. Acad. Sci. 104 (2007) 9139–9144.
[13] J. Ritsema, H.J. Van Heijst, J.H. Woodhouse, Global transition zone tomography, Journal of Geophysical Research: Solid Earth 109 (2004).
[14] K. Hirose, Phase transitions in pyrolitic mantle around 670-km depth: Implications for upwelling of plumes from the lower mantle, Journal of Geophysical Research: Solid Earth 107 (2002) ECV 3-1-ECV 3-13.
[15] M. Akaogi, A. Tanaka, E. Ito, Garnet–ilmenite–perovskite transitions in the system Mg4Si4O12–Mg3Al2Si3O12 at high pressures and high temperatures: phase equilibria, calorimetry and implications for mantle structure, Phys. Earth Planet. Inter. 132 (2002) 303–324.
[16] A. Kubo, M. Akaogi, Post-garnet transitions in the system Mg4Si4O12–Mg3Al2Si3O12 up to 28 GPa: phase relations of garnet, ilmenite and perovskite, Phys. Earth Planet. Inter. 121 (2000) 85–102.
[17] T. Ishii, H. Kojitani, M. Akaogi, Post-spinel transitions in pyrolite and Mg2SiO4 and akimotoite–perovskite transition in MgSiO3: Precise comparison by high-pressure high-temperature experiments with multi-sample cell technique, Earth Planet. Sci. Lett. 309 (2011) 185–197.
[18] E.R. Hernández, J. Brodholt, D. Alfè, Structural, vibrational and thermodynamic properties of Mg2SiO4 and MgSiO3 minerals from first-principles simulations, Phys. Earth Planet. Inter. 240 (2015) 1–24.
[19] Y.G. Yu, R.M. Wentzcovitch, V.L. Vinograd, et al., Thermodynamic properties of MgSiO3majorite and phase transitions near 660 km depth in MgSiO3and Mg2SiO4: A first principles study, J. Geophys. Res. 116 (2011).
[20] C. Zhou, S. Gréaux, N. Nishiyama, et al., Sound velocities measurement on MgSiO3 akimotoite at high pressures and high temperatures with simultaneous in situ X-ray diffraction and ultrasonic study, Phys. Earth Planet. Inter. 228 (2014) 97–105.
[21] D.J. Weidner, E. Ito, Elasticity of MgSiO3 in the ilmenite phase, Phys. Earth Planet. Inter. 40 (1985) 65–70.
[22] T. Yamanaka, Y. Komatsu, M. Sugahara, et al., Structure change of MgSiO3, MgGeO3, and MgTiO3 ilmenites under compression, Am. Mineral. 90 (2005) 1301–1307.
[23] B. Reynard, G. Fiquet, J.-P. Itie, et al., High-pressure X-ray diffraction study and equation of state of MgSiO3 ilmenite, Am. Mineral. 81 (1996) 45–50.
[24] E. Ito, Y. Matsui, Silicate ilmenites and the post-spinel transformations, in: M.H. Manghnani, S.-I. Akimoto (Eds.), High-Pressure Research, Academic Press, New York, 1977, pp. 193–208.
[25] Y. Wang, T. Uchida, J. Zhang, et al., Thermal equation of state of akimotoite MgSiO3 and effects of the akimotoite–garnet transformation on seismic structure near the 660 km discontinuity, Phys. Earth Planet. Inter. 143 (2004) 57–80.
[26] S. Hao, W. Wang, W. Qian, et al., Elasticity of akimotoite under the mantle conditions: Implications for multiple discontinuities and seismic anisotropies at the depth of ~600–750 km in subduction zones, Earth Planet. Sci. Lett. 528 (2019) 115830.
[27] C.R.S. Da Silva, B.B. Karki, L. Stixrude, et al., Ab initio study of the elastic behavior of MgSiO3ilmenite at high pressure, Geophys. Res. Lett. 26 (1999) 943–946.
[28] B.B. Karki, R.M. Wentzcovitch, First-principles lattice dynamics and thermoelasticity of MgSiO3ilmenite at high pressure, Journal of Geophysical Research: Solid Earth 107 (2002) ECV2.1–ECV2.6.
[29] P. Giannozzi, S. Baroni, N. Bonini, et al., QUANTUM ESPRESSO: a modular and open-source software project for quantum simulations of materials, J. Phys. Condens. Matter 21 (2009) 395502.
[30] P. Hohenberg, W. Kohn, Inhomogeneous Electron Gas, Phys. Rev. 136 (1964) B864–B871.
[31] J.P. Perdew, A. Zunger, Self-interaction correction to density-functional approximations for many-electron systems, Phys. Rev. B 23 (1981) 5048–5079.
[32] W. Kohn, L.J. Sham, Self-Consistent Equations Including Exchange and Correlation Effects, Phys. Rev. 140 (1965) A1133–A1138.
[33] B. Karki, R.M. Wentzcovitch, S. De Gironcoli, et al., High-pressure lattice dynamics and thermoelasticity of MgO, Phys. Rev. B 61 (2000) 8793–8800.
[34] D. Vanderbilt, Soft self-consistent pseudopotentials in a generalized eigenvalue formalism, Phys. Rev. B 41 (1990) 7892–7895.
[35] N. Troullier, J.L. Martins, Efficient pseudopotentials for plane-wave calculations, Phys. Rev. B 43 (1991) 1993.
[36] R.M. Wentzcovitch, Invariant molecular-dynamics approach to structural phase transitions, Phys. Rev. B 44 (1991) 2358–2361.
[37] S. Baroni, S. De Gironcoli, A. Dal Corso, et al., Phonons and related crystal properties from density-functional perturbation theory, Rev. Mod. Phys. 73 (2001) 515–562.

[38] T. Barron, M. Klein, Second-order elastic constants of a solid under stress, Proceedings of the Physical Society (1958-1967) 85 (1965) 523–532.
[39] Z. Wu, R.M. Wentzcovitch, Quasiharmonic thermal elasticity of crystals: An analytical approach, Phys. Rev. B 83 (2011) 184115.
[40] Y. Hu, Z. Wu, P.K. Dera, et al., Thermodynamic and elastic properties of pyrope at high pressure and high temperature by first-principles calculations, Journal of Geophysical Research: Solid Earth 121 (2016) 6462–6476.
[41] W. Qian, W. Wang, F. Zou, et al., Elasticity of Orthoenstatite at High Pressure and Temperature: Implications for the Origin of Low VP/VS Zones in the Mantle Wedge, Geophys. Res. Lett. 45 (2018) 665–673.
[42] W. Wang, Z. Wu, Elasticity of Corundum at High Pressures and Temperatures: Implications for Pyrope Decomposition and Al-Content Effect on Elastic Properties of Bridgmanite, Journal of Geophysical Research: Solid Earth 123 (2018) 1201–1216.
[43] D. Yang, W. Wang, Z. Wu, Elasticity of superhydrous phase B at the mantle temperatures and pressures: Implications for 800 km discontinuity and water flow into the lower mantle, Journal of Geophysical Research: Solid Earth 122 (2017) 5026–5037.
[44] F. Zou, Z. Wu, W. Wang, et al., An Extended Semianalytical Approach for Thermoelasticity of Monoclinic Crystals: Application to Diopside, Journal of Geophysical Research: Solid Earth 123 (2018) 7629–7643.
[45] Z. Wu, J.F. Justo, R.M. Wentzcovitch, Elastic anomalies in a spin-crossover system: ferropericlase at lower mantle conditions, Phys Rev Lett 110 (2013) 228501.
[46] D.J. Frost, The Upper Mantle and Transition Zone, Elements 4 (2008) 171–176.
[47] J.F. Lin, S. Speziale, Z. Mao, et al., Effects of the Electronic Spin Transitions of Iron in Lower Mantle Minerals: Implications for Deep Mantle Geophysics and Geochemistry, Rev. Geophys. 51 (2013) 244–275.
[48] A.E. Ringwood, Phase transformations and differentiation in subducted lithosphere: Implications for mantle dynamics, basalt petrogenesis, and crustal evolution, The Journal of Geology 90 (1982) 611–643.
[49] T. Irifune, M. Isshiki, Iron partitioning in a pyrolite mantle and the nature of the 410-km seismic discontinuity, Nature 392 (1998) 702–705.
[50] T. Irifune, T. Shinmei, C.A. Mccammon, et al., Iron partitioning and density changes of pyrolite in Earth's lower mantle, Science 327 (2010) 193–195.
[51] S.S. Sun, Chemical composition and origin of the Earth's primitive mantle, Geochim. Cosmochim. Acta 46 (1982) 179–192.
[52] D. Frost, F. Langenhorst, P. Van Aken, Fe–Mg partitioning between ringwoodite and magnesiowüstite and the effect of pressure, temperature and oxygen fugacity, Phys. Chem. Miner. 28 (2001) 455–470.
[53] D.J. Frost, F. Langenhorst, The effect of Al2O3 on Fe–Mg partitioning between magnesiowüstite and magnesium silicate perovskite, Earth Planet. Sci. Lett. 199 (2002) 227–241.
[54] T. Ishii, H. Kojitani, M. Akaogi, Phase relations and mineral chemistry in pyrolitic mantle at 1600–2200 °C under pressures up to the uppermost lower mantle: Phase transitions around the 660-km discontinuity and dynamics of upwelling hot plumes, Phys. Earth Planet. Inter. 274 (2018) 127–137.
[55] T. Arimoto, S. Gréaux, T. Irifune, et al., Sound velocities of Fe3Al2Si3O12 almandine up to 19 GPa and 1700 K, Phys. Earth Planet. Inter. 246 (2015) 1–8.
[56] R. Hill, The elastic behaviour of a crystalline aggregate, Proceedings of the Physical Society. Section A. 65 (1952) 349–354.
[57] T. Ferroir, P. Beck, B. Van De Moortèle, et al., Akimotoite in the Tenham meteorite: Crystal chemistry and high-pressure transformation mechanisms, Earth Planet. Sci. Lett. 275 (2008) 26–31.
[58] O. Tschauner, C. Ma, C. Prescher, et al., Structure analysis and conditions of formation of akimotoite in the Tenham chondrite, Meteorit. Planet. Sci. 53 (2018) 62–74.
[59] T. Irifune, A. Ringwood, Phase transformations in a harzburgite composition to 26 GPa: implications for dynamical behaviour of the subducting slab, Earth Planet. Sci. Lett. 86 (1987) 365–376.
[60] T. Ishii, H. Kojitani, M. Akaogi, Phase Relations of Harzburgite and MORB up to the Uppermost Lower Mantle Conditions: Precise Comparison With Pyrolite by Multi-sample Cell High-Pressure Experiments With Implication to Dynamics of Subducted Slabs, Journal of Geophysical Research: Solid Earth 124 (2019) 3491–3507.
[61] S. Goes, R. Agrusta, J. Van Hunen, et al., Subduction-transition zone interaction: A review, Geosphere 13 (2017) 644–664.
[62] P.E. Van Keken, B.R. Hacker, E.M. Syracuse, et al., Subduction factory: 4. Depth-dependent flux of H2O from subducting slabs worldwide, J. Geophys. Res. 116 (2011).
[63] E.M. Syracuse, P.E. Van Keken, G.A. Abers, The global range of subduction zone thermal models, Phys. Earth Planet. Inter. 183 (2010) 73–90.
[64] S.J. Chang, A.M.G. Ferreira, Inference on Water Content in the Mantle Transition Zone Near Subducted Slabs From Anisotropy Tomography, Geochemistry, Geophysics, Geosystems 20 (2019) 1189–1201.
[65] K. Visser, J. Trampert, S. Lebedev, et al., Probability of radial anisotropy in the deep mantle, Earth Planet. Sci. Lett. 270 (2008) 241–250.
[66] S.W. French, B.A. Romanowicz, Whole-mantle radially anisotropic shear velocity structure from spectral-element waveform tomography, Geophys. J. Int. 199 (2014) 1303–1327.
[67] W. Wu, S. Ni, J.C. Irving, Inferring Earth's discontinuous chemical layering from the 660-kilometer boundary topography, Science 363 (2019) 736–740.
[68] Y. Fukao, M. Obayashi, Subducted slabs stagnant above, penetrating through, and trapped below the 660 km discontinuity, Journal of Geophysical Research: Solid Earth 118 (2013) 5920–5938.
[69] A. Akashi, Y. Nishihara, E. Takahashi, et al., Orthoenstatite/clinoenstatite phase transformation in MgSiO3at high-pressure and high-temperature determined by in situ X-ray diffraction: Implications for nature of the X discontinuity, J. Geophys. Res. 114 (2009).

Yajie Zhao is a Ph.D. candidate in School of Earth and Space Sciences, University of Science and Technology of China. She got her Bachelor's degree in geophysics from Jilin University in 2019. Her research interests focus on elastic properties of minerals which are calculated by first-principles calculations under the condition of high pressure and temperature.

Zhongqing Wu is Professor in School of Earth and Space Sciences, University of Science and Technology of China. His group mainly focuses on the composition and structure of the deep Earth's interior using the properties of minerals at high pressure and temperature from first-principles calculations.